nature photonics

REVIEW ARTICLE

PUBLISHED ONLINE: 1 SEPTEMBER 2017 | DOI: 10.1038/NPHOTON.2017.142

# Fano resonances in photonics

Mikhail F. Limonov[1,2], Mikhail V. Rybin[1,2*], Alexander N. Poddubny[1,2] and Yuri S. Kivshar[2,3]

**Rapid progress in photonics and nanotechnology brings many examples of resonant optical phenomena associated with the physics of Fano resonances, with applications in optical switching and sensing. For successful design of photonic devices, it is important to gain deep insight into different resonant phenomena and understand their connection. Here, we review a broad range of resonant electromagnetic effects by using two effective coupled oscillators, including the Fano resonance, electromagnetically induced transparency, Kerker and Borrmann effects, and parity–time symmetry breaking. We discuss how to introduce the Fano parameter for describing a transition between two seemingly different spectroscopic signatures associated with asymmetric Fano and symmetric Lorentzian shapes. We also review the recent results on Fano resonances in dielectric nanostructures and metasurfaces.**

We live in a world of resonances. The human environment is filled with natural and artificial resonators, ranging from musical instruments to complex devices such as lasers and body-imaging machines. Resonances are the cornerstone of photonics, with the more familiar Fabry–Pérot and Bragg resonators employed as building blocks for sophisticated optical devices with unique properties. A very special example of a resonance in optics is the Fano resonance that occurs when a discrete localized state becomes coupled to a continuum of states. Although the paper by Ugo Fano was published in *Physical Reviews* in 1961[1], the original results for an important limiting case appeared back in 1935[2].

In general, the Fano resonance occurs when a discrete quantum state interferes with a continuum band of states, and it is manifested in the absorption spectrum, $\sigma(E)$, with the shape described by the famous Fano formula:

$$\sigma(E) = D^2 \frac{(q+\Omega)^2}{1+\Omega^2} \qquad (1)$$

where $E$ is the energy, $q = \cot\delta$ is the Fano parameter, $\delta$ is the phase shift of the continuum, $\Omega = 2(E - E_0) / \Gamma$, where $\Gamma$ and $E_0$ are the resonance width and energy, respectively, and $D^2 = 4\sin^2\delta$ (in the form presented in ref. 3). Equation (1) turns out to be generally applicable not only to absorption but also to different optical spectra (including transmission and scattering) in a variety of systems. In recent years, Fano resonance has attracted a lot of attention due to the progress in photonics, which deals with objects that have multiple resonances. Indeed, almost any resonant state can be considered as quasi-discrete with a complex frequency that can be described in terms of Fano resonance. We note that the major interest in the study of Fano resonances in photonics originates from sharp transmission–reflection curves supplied by this resonance, with a sharp transition from the total transmission to reflection. This is an attractive feature that underpins concepts of many switching devices in photonics.

To provide an example of a resonance with the characteristic Fano response, we consider the elastic Mie scattering of electromagnetic waves by a high-index dielectric rod. Figure 1 summarizes the unique properties of the Fano resonance in this case, and it also demonstrates why the Fano resonance is so important for numerous applications in photonics. Indeed, the study of the resonant Mie scattering by a dielectric rod reveals[4–6] that the scattering spectra can be presented as an infinite series of Fano resonances. The unique feature of the Fano formula is that the scattering efficiency described by equation (1) has two critical points: when the scattering efficiency vanishes and when it takes the maximum value close to unity. This feature is useful for many applications, allowing the scattering to be switched from total reflection to total transmission. Indeed, for a particular normalized frequency ($x = 0.504$ in Fig. 1), the resonant field $H_z$ near the surface

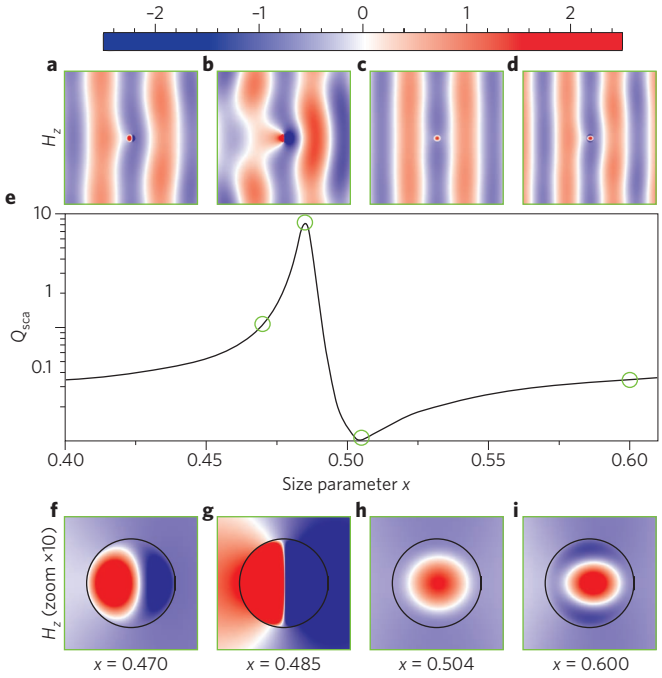


**Figure 1 | Fano resonances in Mie scattering. a–i**, Numerical results for Mie scattering by a single dielectric rod ($\varepsilon = 60$) embedded in air ($\varepsilon = 1$) are shown for the scattering efficiency, $Q_{sca}$. The component $H_z$ of the transverse-electric electromagnetic field is shown for the selected points outside (**a**–**d**) and inside (**f**–**i**) a dielectric rod marked by the green circles in **e**. Shown are strong Mie scattering at $x = 0.485$ (**b**,**g**) and Fano invisible regime at $x = 0.504$ (**c**,**h**). Here $x = r\omega / c$, and $r$ is the rod radius and $c$ the speed of light.

[1]Ioffe Institute, St. Petersburg 194021, Russia. [2]ITMO University, St. Petersburg 197101, Russia. [3]Nonlinear Physics Center, Australian National University, Canberra, Australian Capitial Territory 2601, Australia. *e-mail: m.rybin@mail.ioffe.ru

inside the rod mimics the incident field distribution, so we observe almost complete suppression of scattering. This means that an incident transverse-electric-polarized light passes the rod almost without scattering, and the rod becomes invisible for any angle of observation without additional coating layers.

In atomic spectroscopy, the minimum in the Fano response function is usually referred to as the 'resonance window', to avoid confusion with other types of minima in the absorption cross-section[3,7]. In photonics, the characteristic windows in the transmission or absorption spectra can also be observed in the case of different regimes caused, for example, by the Borrmann effect[8–10] or by the optical analogue of electromagnetically induced transparency (EIT)[11–15]. To further deepen our understanding of the physics of Fano resonance, we need to answer the following question: How can we distinguish between Fano resonance and other resonances in experimental data or calculated spectra? A more general question is: How do we prove that an asymmetric or even symmetric feature in the spectrum originates from Fano resonance? In the past decade, we have observed a growing number of publications mentioning Fano resonance. However, many authors call almost any feature observed in the spectrum 'Fano resonances' without giving a rigorous proof. Below, we provide the basic tools to prove the existence of Fano resonances in any system.

One of the goals of this Review is to present a general picture of different resonant photonic effects (Fano, Kerker, Borrmann, EIT) based on a simple model of two weakly coupled oscillators. Next, we provide a detailed analysis of the Fano asymmetry parameter $q$, which is the key characteristic of the Fano theory. By analysing experimental data or numerical spectra, it is possible to extract different expressions for the response function and compare them with the expected form of the Fano formula.

It is crucially important that the Fano formula (equation (1)) is useful for describing resonant phenomena in a broad range of systems, including optomechanical resonators[16], semiconductor nanostructures[17,18], superconductors[19,20], photonic crystals[21–26], dielectric nanoparticles[27], plasmonic nanoantennas[28–34], and many others. In nanophotonics, the Fano resonance was initially introduced and observed for plasmonic structures. However, for such structures, ohmic losses and heating limit performance in many optical devices. For this reason, several research teams have turned their attention to the study of all-dielectric metamaterials[35–40] with considerably lower losses, and also metasurfaces, which are two-dimensional (2D) successors of metamaterials[41–45]. These two classes of photonic structures are the main focus of this Review.

In addition, we emphasize that Fano resonance and associated effects have been found in very recent studies related to photonics. Using spectral features of the resonant lineshape, Fano physics can help to achieve negative optical scattering force for nanoparticles[46], reveal bound states in the continuum[47,48] and exotic states of subwavelength topological photonics[49], as well as realize a variety of useful applications[50–57]. We believe this Review will provide useful guidelines for future, not yet discovered manifestations of Fano resonances and their novel applications.

## Two coupled oscillators and a phase diagram

Here we illustrate the physics of Fano resonances, optical EIT, and Borrmann and Kerker effects, as well as parity–time symmetry breaking by using a model of two coupled driven oscillators[12,58–61] described by the following matrix equation:

$$\begin{pmatrix} \omega_1 - \omega - i\gamma_1 & g \\ g & \omega_2 - \omega - i\gamma_2 \end{pmatrix} \begin{pmatrix} x_1 \\ x_2 \end{pmatrix} = i \begin{pmatrix} f_1 \\ f_2 \end{pmatrix} \quad (2)$$

Here $x_1$ and $x_2$ are the oscillator amplitudes, $\omega_1$ and $\omega_2$ are the resonant frequencies, $\gamma_1$ and $\gamma_2$ are the damping coefficients, and $f_1$ and $f_2$ are the external forces with the driving frequency $\omega$. The coupling constant $g$ describes the interaction between the oscillators.

Various resonant effects possible in such system, optical realizations and characteristic spectra are summarized in Box 1. We will now analyse them in a unified fashion by comparing the values of the damping constants $\gamma_1$ and $\gamma_2$ as shown in the phase diagram (Fig. 2). The damping constants are normalized by the absolute value of the coupling parameter $g$ between the oscillators. The physical origin of the dampings can be ohmic losses or scattering losses due to coupling to other modes. In the weak-coupling regime, the coupling strength is less than one of the dampings, $|g| << |\gamma_1|$ or $|g| << |\gamma_2|$ (ref. 62). Then the interaction between the oscillators slightly shifts their complex eigenfrequencies, for example, $\omega_1' \approx \omega_1 - i\gamma_1 + \Delta\omega_1$ is the eigenfrequency of oscillator 1 modified due to the interaction with oscillator 2 characterized by a complex shift $\Delta\omega_1$. In the case when the first oscillator emulates a quantum emitter and the second oscillator corresponds to a photonic mode of a cavity, the imaginary part of $\Delta\omega_1$ describes the Purcell effect[63], that is, modification of the spontaneous emission rate in the cavity. The real part of $\Delta\omega_1$ is the radiative correction to the eigenfrequency being analogous to the Lamb shift[64].

**Fano resonance.** This resonance is realized in the two-oscillator model in the weak-coupling regime when only one of the oscillators (with larger damping) is driven (namely, $f_1 \neq 0, f_2 = 0$; see the inset of Fig. 2 for a mechanical analogy). This corresponds to the two sectors of the first quadrant of the phase diagram (Fig. 2) close to the axes, shown in red. The amplitude of the driven oscillator 1 in the spectral vicinity of the resonance of oscillator 2 can be presented in the form:

$$|x_1(\Omega)|^2 \approx |f_1^2| \frac{\gamma_1^2}{(\omega_1 - \omega_2)^2 + \gamma_1^2} \frac{(\Omega + q)^2}{(\Omega^2 + 1)}$$

where

$$\Omega = \left[ \omega - \omega_2 + \left( \frac{g^2}{\gamma_1} \right) \frac{(\omega_1 - \omega_2)}{1 + q^2} \right] \frac{\gamma_1 (1 + q^2)}{g^2}$$

is the dimensionless frequency. The Fano parameter $q$ determines the spectral shape and depends on the spectra detuning of the oscillators $\omega_2 - \omega_1$. Similar to equation (1), $q = \cot\delta$, where $\delta$ is the phase of the response function $(\omega_2 - \omega_1 + i\gamma_1)^{-1}$ of the damped oscillator 2, playing the role of continuum at the resonance of oscillator 1. The Fano resonance directly manifests itself in the absorption spectrum $\propto \gamma_1 |x_1(\Omega)|^2$ (Box 1, panel b). For two ring resonators side-coupled to the waveguide, the absorbed waves are subtracted from the transmission, which leads to Fano-like transmission spectra[11].

**Electromagnetically induced transparency.** EIT can be viewed as a special case of Fano resonance when the frequencies of strongly and weakly damped oscillators match, $\omega_1 = \omega_2$, so that $q = 0$, as explained in Box 1.

**Borrmann effect.** This effect is an anomalously strong transmission of waves through an absorbing crystal due to the Bragg diffraction[8–10,65,66]. It is similar to EIT but should be described in the spatial domain rather than in the time domain, which means that the frequencies are to be replaced by wave numbers, $\omega \to k$. Namely, $x_1$ and $x_2$ become the amplitudes of the left and right propagating plane waves, with $\omega_1 = -\omega_2$ and $\omega$ being their wave vectors and the Bloch wave vector calculated from the edge of the Brillouin zone. The coupling coefficient $g$ appears due to the Bragg diffraction. The damping constants $\gamma_1 = -\gamma_2$ describe the wave attenuation due to absorption and they have opposite signs because the left and right propagating

**Box 1 | Resonant phenomena in photonics realized for different coupling regimes.**

**Weak-coupling regime: $|g|<<|\gamma_1|$ or $|g|<<|\gamma_2|$**

*Fano resonance.* Fano resonance occurs from coupling of two oscillators with strongly different damping rates producing narrow and broad spectral lines. The coupling constant $g$ is weaker than the larger damping $\gamma$. The phase of the undamped oscillator changes by $\pi$ at the resonance ('+' and '−' signs in panel **a**), while the phase of the strongly damped oscillator varies slowly (a pair of '+' signs). The resulting spectra (panel **b;** adapted from ref. 1, APS) show typical asymmetry with a sharp change between a dip and a peak. The spectral shape depends on the phase shift $\delta$ between the oscillators encoded in the Fano parameter $q$ (panel **b**).

*Electromagnetically induced transparency.* EIT can be viewed as a Fano resonance at $\omega_1 = \omega_2$, when the $q$ parameter vanishes. Usually, the resonant mode with larger damping is manifested as a wide stop band in transmission. However, the transmission can be resonantly restored by the coupling to the undamped mode with the opposite phase, cancelling the losses out (panel **c**). This results in a narrow transparency window as shown in panel **d** (reproduced from ref. 11, Macmillan Publishers Ltd).

*Borrmann effect.* This effect is a spatial analogue of EIT for a structure with a periodic loss distribution. At the bandgap edge, the Bragg diffraction pins the field maxima to the lossless material (red in panel **e**) away from the lossy one (blue in panel **e**). This suppresses the losses and opens the transparency window (experimental and theoretical data correspond to red dotted and black solid curves in panel **f**, respectively; adapted from ref. 65, OSA).

*Kerker effect.* This effect is distinct from the Fano resonance because it does not require direct coupling between the oscillating modes but exploits their different spatial symmetry instead. Namely, electric dipole (ED) and magnetic dipole (MD) modes are odd (even) with respect to the spatial inversion (panel **g**). Hence, it is possible to suppress light scattering either in backward (Kerker 1 condition) or forward (Kerker 2) directions when the MD phase changes by $\pi$ at resonance. Scattering patterns are shown in panel **h** (adapted from ref. 67, APS).

**Strong-coupling regime: $|g|>>|\gamma_1|$ and $|g|>>|\gamma_2|$**

*Rabi splitting or Autler–Townes effect.* This is seen in the strong-coupling regime when the oscillators exchange their energy much faster than it leaks away. Two coupled eigenmodes form and their frequencies split from those of non-interacting oscillators (panel **i**). The transmission maximum between split modes (panel **j**; adapted from ref. 11, Macmillan Publishers Ltd) is reminiscent of the EIT window (panel **d**) but has a different origin: it is unrelated to loss cancellation. (The red dashed lines in panel **j** are guides for the resonant energy.)

*Parity–time symmetry.* Parity–time symmetry is an analogue of the strong-coupling regime for systems that are symmetric under simultaneous spatial and time inversion, where the gain is balanced by losses ($\gamma_1 = -\gamma_2$, $\omega_1 = \omega_2$). Despite the non-Hermitian properties, the spectrum is real and the real parts of eigenfrequencies split when the coupling overcomes gain/loss ($g > |\gamma_1|$; panel **k**). When the coupling is weak, the parity–time symmetry is broken and the spectrum is complex with a large gain–loss contrast. In particular, this facilitates single-mode lasing: only the mode pinned to the gain regions is above the lasing threshold, akin to the Borrmann effect (panel **l**; adapted from ref. 73, AAAS); $m$ is the azimuthal mode order.

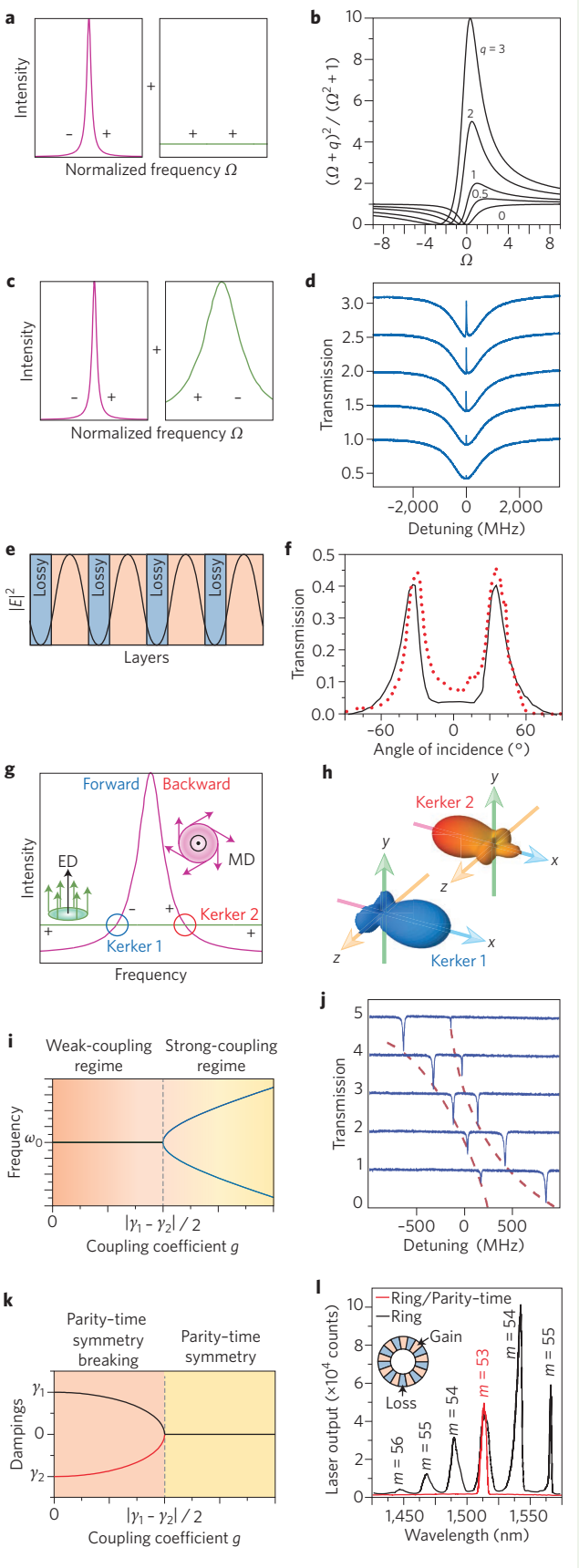

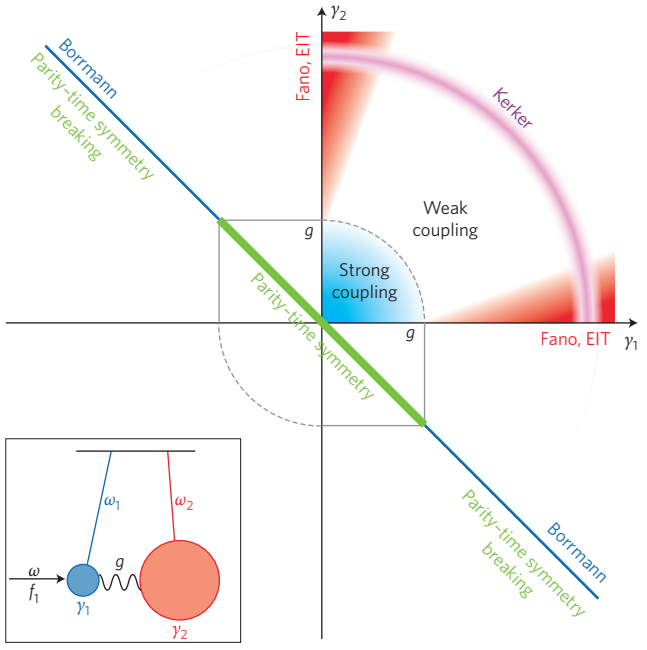


**Figure 2 | Phase diagram of different photonic resonances (Fano, EIT, Kerker, Borrmann, parity–time symmetric) in the damping constants ($\gamma_1$, $\gamma_2$) plane.** Inset: schematic view of two coupled damped oscillators with a driving force $f_1$ applied to one of them.

waves decay in the opposite directions. Hence, the Borrmann effect occupies the line $\gamma_1 = -\gamma_2$ in the phase diagram of Fig. 2.

The transmission coefficient can be estimated as $|t|^2 \propto \exp(-2L|\mathrm{Im}(\omega_\pm)|)$, where $L$ is the dimensionless structure length and the Bloch vectors $\omega_\pm$ are defined by the eigenvalues of the system equation (2), $\omega_\pm(\omega_1) = \mp[(\mathrm{Im}(g) - \omega_1)(-\mathrm{Im}(g) + 2i\gamma_1 - \omega_1)]^{1/2}$. As such, the transmission decays when $\mathrm{Im}(\omega) \neq 0$. However, at the particular frequency, when the nodes of the electric field lie within the lossy regions, the absorption is suppressed (Box 1, panel e). Mathematically, this means that the off-diagonal complex coefficients in the matrix of equation (2) cancel each other for $\omega_1 = \mathrm{Im}(g)$, so that $\mathrm{Im}(\omega) = 0$ and the transmission is restored, $|t| \approx 1$, resembling the case of EIT (Box 1, panel f).

**Kerker effect.** Non-trivial effects can be observed even in the limit of vanishing direct coupling between the oscillators, just due to the interference of their independent responses to the external field. As an example, we mention the Kerker effect, defined as cancellation of the scattering amplitude from spherical particles due to the different spatial symmetry of electric and magnetic dipole scattering[67–70]. In the model equation (2), the Kerker effect corresponds to negligible coupling $g = 0$ and equal excitation amplitudes $f_1 = f_2$. In contrast to the Fano and EIT regimes, both oscillators can interact with the field directly ($f_1 \neq 0, f_2 \neq 0$) and also the ratio of their damping rates can be arbitrary. Hence, the Kerker regime occupies the whole region $\gamma_1,\gamma_2 >> g$ in the phase diagram (shown in purple in Fig. 2). There are two Kerker conditions, leading to the scattering suppression in either the forward or backward direction when $x_1 = x_2$ or $x_1 = x_2^*$, respectively (Box 1, panels g and h).

**Strong-coupling regime.** This regime is realized when the dampings of both oscillators are weak, $\gamma_1,\gamma_2 << g$. Hence, in contrast to the Fano, EIT and Kerker regimes, the strong coupling corresponds to the central region of the phase diagram (Fig. 2). In the strong-coupling regime, the real parts of the eigenfrequencies of the system of two coupled oscillators are split by $|\omega_+ - \omega_-| \approx 2g$ when the bare oscillator frequencies $\omega_1$ and $\omega_2$ are tuned to each other. This splitting is termed vacuum Rabi splitting[62,71,72] or Autler–Townes splitting[11] in analogy with quantum optics. Importantly, while the real parts of $\omega_+$ and $\omega_-$ split at $g = |\gamma_1 - \gamma_2| / 2$ (Box 1, panel i), this splitting can be spectrally resolved only when it exceeds the imaginary parts of the eigenfrequencies, that is, $g >> \gamma_1,\gamma_2$, which is the true strong-coupling condition. In the system of ring resonators coupled to the waveguide, the transmission is suppressed at the eigenfrequencies $\omega_\pm$ and restored between them. The transmission spectrum can then be confused with that in the EIT regime (panels j and d in Box 1). However, the physical origin of the central transmission maximum is quite different. In the strong-coupling case, the resonators are not excited at the central frequency, whereas in the EIT case, the central frequency corresponds to the resonant excitation of the weakly damped resonator. The experimental fingerprint of the strong-coupling regime is the avoided crossing of the spectral resonances[11,65], observed when the oscillator frequencies are tuned with respect to each other.

**Parity–time symmetry.** A non-Hermitian system with balanced gain and loss, that is, $\omega_1 = \omega_2$ but opposite coefficients, $\gamma_1 = -\gamma_2$, can exhibit parity–time symmetry[73–76]. As such, parity–time-symmetric structures occupy the line crossing the second and fourth quadrants of the phase diagram (Fig. 2). When $|\gamma_1| < g$, both eigenfrequencies $\omega_\pm$ are real despite the presence of loss and gain (Box 1, panel k). For sufficiently strong loss and gain ($|\gamma_1| > g$), the parity–time symmetry breaks down, and both eigenfrequencies acquire non-zero and opposite imaginary parts, as dictated by the properties of non-interacting oscillators. Hence, the parity–time-symmetric and the parity–time-symmetry-broken regime can be viewed as the strong-coupling and the weak-coupling regimes, respectively, of the particular non-Hermitian system. Balanced gain and loss facilitate single-mode lasing in the parity–time-symmetry-broken regime: only the mode pinned to the gain regions is above the threshold[73]. In periodic structures, this is strongly reminiscent of the Borrmann effect discussed above. Such correspondence between the Borrmann effect and the parity–time symmetry is clearly seen in the phase diagram (Fig. 2). This has been uncovered only recently in the context of topological edge states[77,78]. The conventional photonic crystal with a periodic array of lossy elements is mapped to the parity–time-symmetric photonic crystal with periodic gain and loss elements just by adding an effective homogeneous gain (panels e and l in Box 1). It is worth noting that in the linear regime, the parity–time structure remains reciprocal and the forward and backward transmission coefficients are equal[79]. Nonreciprocal transmission can be realized in the nonlinear regime[76,80].

To summarize this general classification of resonant effects, we note that their variety extends far beyond the model of two coupled oscillators represented in equation (2). For example, scattering from complex structures such as dielectric oligomers characterized by the Fano effect can be analysed conveniently in terms of the interference between the collective eigenmodes of particles, rather than resonances of individual particles. This interference occurs due to non-Hermitian properties of open optical systems, and it can lead to strongly asymmetric spectral lineshapes[81].

## Proving the existence of Fano resonance

A simple tool to reveal the Fano resonance in a considered photonic structure is to develop and study a simple theoretical model that describes the major spectral properties[4,82–86]. Another approach is to decompose the spectrum and fit the spectral line with the Fano formula (equation (1)) by varying different available parameters. Below, we employ both these approaches for analysing the Fano resonance in several examples of dielectric photonic structures. We discuss in detail how to extract the key Fano parameter $q$ characterizing the specific asymmetric profile of the Fano response function (Fig. 3), being responsible for the coupling strength between

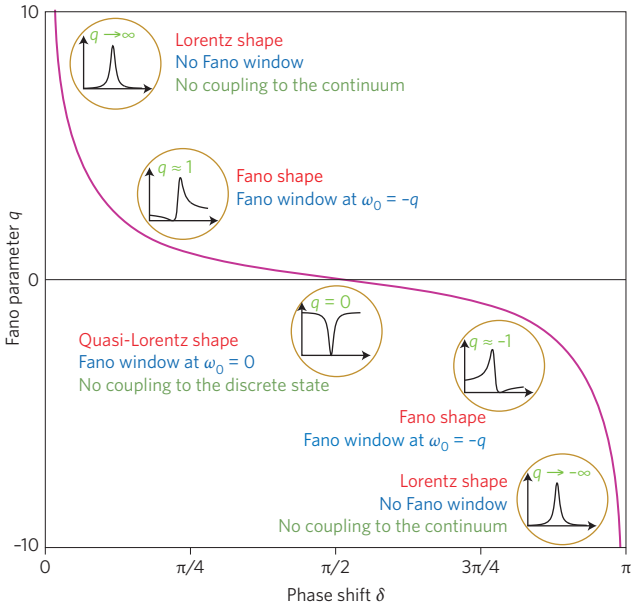


**Figure 3 | Fano parameter versus phase shift and the Fano response function.** Function $q(\delta)$ is periodic in π. The insets show the Fano lineshapes $\sigma(\omega)$ from equation (1) for selected values of $q(\delta)$. The Fano function $\sigma(\omega)$ has a Lorentzian lineshape for the extreme cases of $\delta \to n\pi$ (integer $n$) corresponding to $q \to +\infty$ and $q \to -\infty$. For $\delta = (n + 1/2)\pi$, $q = 0$, the Fano profile has symmetric quasi-Lorentzian lineshape (a Fano window).

effective discrete and continuum states as well as relative excitation strengths associated with these two states.

The Fano parameter $q$, being a cotangent of the phase shift $\delta$ between two modes, depends on geometric and material parameters of the system and incident waves. There is no general rule how to design a system with a desired value of this parameter. Moreover, the Fano parameter should be regarded as an indicator of the Fano resonance features in the system under study. However, one can suggest an ad hoc procedure for tuning the system parameters and the resulting Fano parameter to achieve a certain value.

If an external perturbation does not couple to the continuum of states, we obtain $q \to \pm\infty$ and the Fano lineshape becomes a symmetric Lorentzian function (Fig. 3). When the external perturbation does not couple to the discrete state, the Fano profile becomes a symmetric quasi-Lorentzian anti-resonance in the continuum spectrum ($q = 0$), and it appears as a true zero in the spectrum. However, this minimum does not vanish and its value grows progressively when more continuum states become involved in the scattering process. The background component that does not interfere with the narrow band can be accounted for by introducing an interaction coefficient $\eta \in [0...1]$ (ref. 67):

$$\sigma(\Omega) = D^2\left[\frac{(q+\Omega)^2}{1+\Omega^2}\eta + (1-\eta)\right]$$

**0D dielectric spheres and rods.** In 1908, Gustav Mie published an analytical solution of Maxwell's equations for the scattering of electromagnetic waves by a spherical particle[87]. In 2008 (exactly 100 years later), the similarity of the Mie scattering in optics and Fano resonances in quantum physics was pointed out[88]. In 2013, it was proven that the well-known resonant Mie scattering from high-contrast dielectric resonators results in an infinite series of Fano resonances[5]. The conclusion was made for the case of dielectric rods[4–6] and recently for dielectric spheres[84,85] and core–shell dielectric particles[89]. For a dielectric rod, it was demonstrated numerically[4,5] that each partial scattered wave can be presented as a sum of two contributions: one of them corresponds to the non-resonant-background scattering while the other is associated with the excitation of a resonant Mie mode. Their interference leads to a typical asymmetric Fano resonance profile[5]. The calculated $q$ values show a general cyclic cotangent-type dependence with a certain phase[5] (Fig. 4d). For dielectric homogeneous and core–shell spheres, the Fano resonance was proved analytically[84,85,89] (Fig. 4b).

**1D disordered structures.** Fano resonances are usually associated with coherent scattering in regular structures, but experimental and theoretical results demonstrate that such resonances may survive in some structures with disorder[83,90,91] as well as in aperiodic photonic systems such as quasi-crystals[92].

A remarkable example of a disorder-induced Fano resonance is observed in a 1D system composed of alternating A and B layers with permittivity $\varepsilon_A$ and random permittivity $\varepsilon_B$ in B layers[83,93] (Fig. 4e). Owing to ergodicity, Fano resonance is a fingerprint feature for any realization of a structure with a certain degree of disorder. The background extinction is determined by uncompensated Fabry–Pérot scattering on different B layers. Depending on the values of the dispersion parameter $\sigma_{\varepsilon_B}$ and the order of the band $h$, the shape of the Bragg reflecting band changes in accord with the Fano formula, namely it transforms from a Bragg stop band to Bragg pass band. The Fano nature of the resonance was proved both numerically and analytically. Figure 4f presents a cotangent-type behaviour (with a certain phase) of the Fano parameter $q$ for third-order Bragg bands.

When the nodes of the electric field are centred at the B layers, the wave is insensitive to the fluctuations of $\varepsilon_B$, and it does not decay (Bragg pass band or Fano window with $q = 0$). This can be interpreted as the Borrmann effect generalized to disordered systems[83].

**2D cavities in waveguides.** One of the typical designs to achieve the Fano resonance in the waveguide geometry is to couple the guided modes to local defects or cavities[94,95]. In the case of a side-coupled cavity (Fig. 4g), an analytical expression for the transmission intensity can be presented in the form of the Fano formula[86]. In such a system, the background amplitude does not change its phase monotonically. As a result, the Fano parameter $q$ does not follow the characteristic cotangent-type dependence, but instead it has the sine-type dependence shown in Fig. 4h.

**3D photonic structures.** There are many examples of Fano resonances in different types of photonic crystal. Opals represent the well-known example of 3D photonic crystals composed of nearly spherical particles of amorphous silica (a-$SiO_2$) (Fig. 4i). The porosity of the a-$SiO_2$ particles produces inhomogeneity of dielectric permittivity of a single a-$SiO_2$ particle. Dissimilarity in the permittivity of a-$SiO_2$ particles leads to the disorder-induced broad background Mie scattering. A narrow photonic Bragg band interacts with the continuum spectrum through an interference effect constructively or destructively leading to Fano resonance[90]. Opals have an overlapping net of air voids in between the a-$SiO_2$ particles, which allows one to infill the voids with various materials[93,96]. Experimental results clearly indicate a remarkable transformation of the Bragg band when the filler permittivity is changed. By changing the filler permittivity, one can change the value of the parameter $q$ (Fig. 4j), for example, switch the Fano-induced asymmetric Bragg stop band into a symmetric Lorentzian pass band and vice versa, and thus control the wave transmission.

Strongly disordered photonic crystals with random scatterers[91] were created from a 3D opal-like structure where disorder appears due to vacancies in a face-centred cubic lattice (Fig. 4k). It was shown that the amount of vacancies not only determines the intensity but

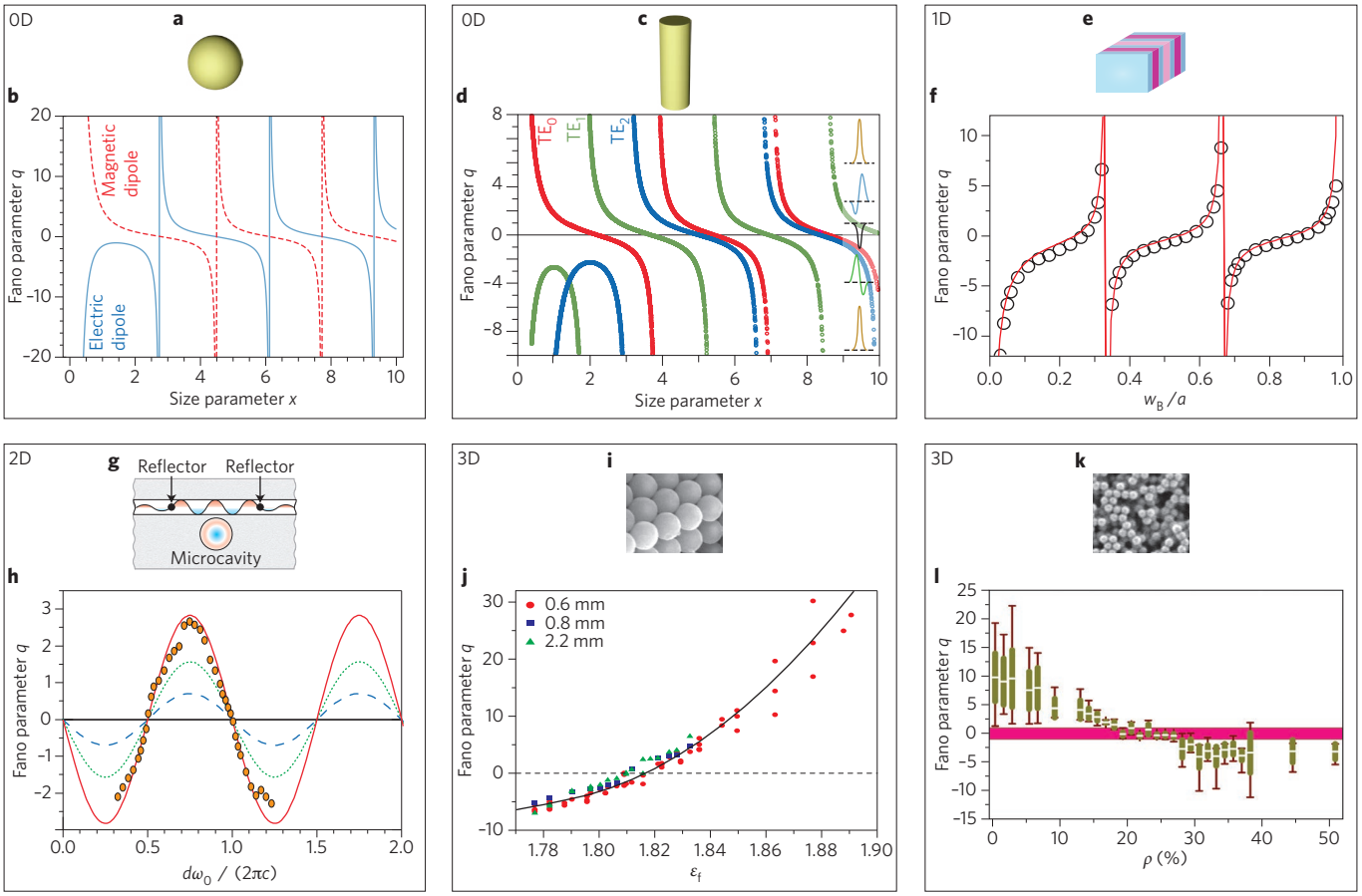


**Figure 4 | Photonic systems and Fano parameter *q*.** **a**, Dielectric homogeneous sphere. **b**, Fano parameter for dielectric sphere depending on the size parameter $x = 2\pi r/\lambda$. **c**, Dielectric homogeneous circular rod. **d**, Fano parameter for the transverse electric $TE_0$ (red), $TE_1$ (green) and $TE_2$ (blue) modes for a circular rod at $\varepsilon_1 = 50$. **e**, 1D structure composed of alternating A and B layers with random permittivity in B layers. **f**, Fano parameter for third-order Bragg bands. Lines and symbols present $q$, calculated analytical and extracted from numerical spectra, respectively. $w_B/a$ is the ratio of the thickness of the B layers to the period. **g**, A waveguide structure with a high-$Q$ side-coupled cavity and a pair of reflectors forming a low-$Q$ Fabry–Pérot resonator. **h**, Fano parameter calculated for $r^2 = 0.1$ (dashed blue), $r^2 = 0.3$ (dotted green) and $r^2 = 0.5$ (solid red). Circles are the values obtained from fitting of the spectra calculated directly for the photonic crystal circuit. $d$ is the distance between reflectors, $w_0$ is the microcavity frequency and $c$ is the speed of light. **i**, Scanning electron microscopy (SEM) image of opal sample. **j**, Fano parameter as a function of the filler permittivity, $\varepsilon_f$, calculated from experimental spectra for three samples with different thickness. The solid line is a guide for the eye. **k**, SEM image of vacancy-doped opal-based photonic crystal for a 50% of vacancy doping. **l**, Fano parameter as a function of the vacancies for different number of layers comprising all the thicknesses measured: from 1 to over 30 monolayers. $\rho$ is the fraction of missing spheres. Figure reproduced from: **b**, ref. 84, APS; **d**, ref. 5, OSA; **f**, ref. 83, Macmillan Publishers Ltd; **g**,**h**, ref. 86, under a Creative Commons licence (http://creativecommons.org/licenses/by/4.0/); **i**, ref. 96, Macmillan Publishers Ltd; **j**, ref. 90, APS; **k**,**l**, ref. 91, courtesy of C. López.

also the nature of the light scattering. The disorder-induced extra scattering produces a background spectrum with a narrow Bragg band superimposed onto this background, with Fano resonance. As the amount of defects varies, light scattering undergoes a transition that very closely resembles the Bragg band transformation observed in the transmission spectra of synthetic opals[90]. The usual Bragg peak changes into a Bragg dip, which can be readily described with the Fano parameter $q$. When the disorder level reaches the percolation threshold, the Fano parameter $q$ changes its sign (Fig. 4l), signalling the transition from a crystal to a mosaic of microcrystals through a state where scattering is maximum. Beyond that point, the system re-enters a state of low scattering with the normal Bragg diffraction[91].

## Fano resonances and metasurfaces

Here we review examples of Fano resonances in the 2D counterpart of metamaterials known as metasurfaces.

**Lattices of nanospheres.** As demonstrated above, a single sphere and a 3D metacrystal composed of spheres can both support Fano resonances of different nature (Fig. 4). Therefore, we can expect that an array of such spheres (also called a metasurface) can have similar properties. Indeed, Fano resonances have been observed for metasurfaces composed of single and coated spheres that form a simple square lattice[97], and 2D periodic arrays of nanoparticle oligomers[98] or circular nanoclusters[99]. Importantly, the Mie scattering from individual spheres can demonstrate Fano resonances as well. Here, we are interested in cooperative effects due to a 2D geometry. Indeed, an array-induced Fano resonance was found for a planar metasurface of plasmonic nanoparticles under oblique plane-wave incidence[97]. Absorption of the ordered arrays of coated spheres is shown in Fig. 5a for both transverse-electric- and transverse-magnetic-polarized plane waves under the oblique incidence with two distinct types of resonance. The first spectral feature is related to the electric dipolar Mie resonance of a single coated sphere (at 1,750 and 2,400 THz). The authors of ref. 97 clarify that the other feature in transverse-magnetic-polarization at 2,050 and 2,800 THz is due to the forced excitation of free modes with a small attenuation constant that is an array-induced sharp Fano collective resonance.

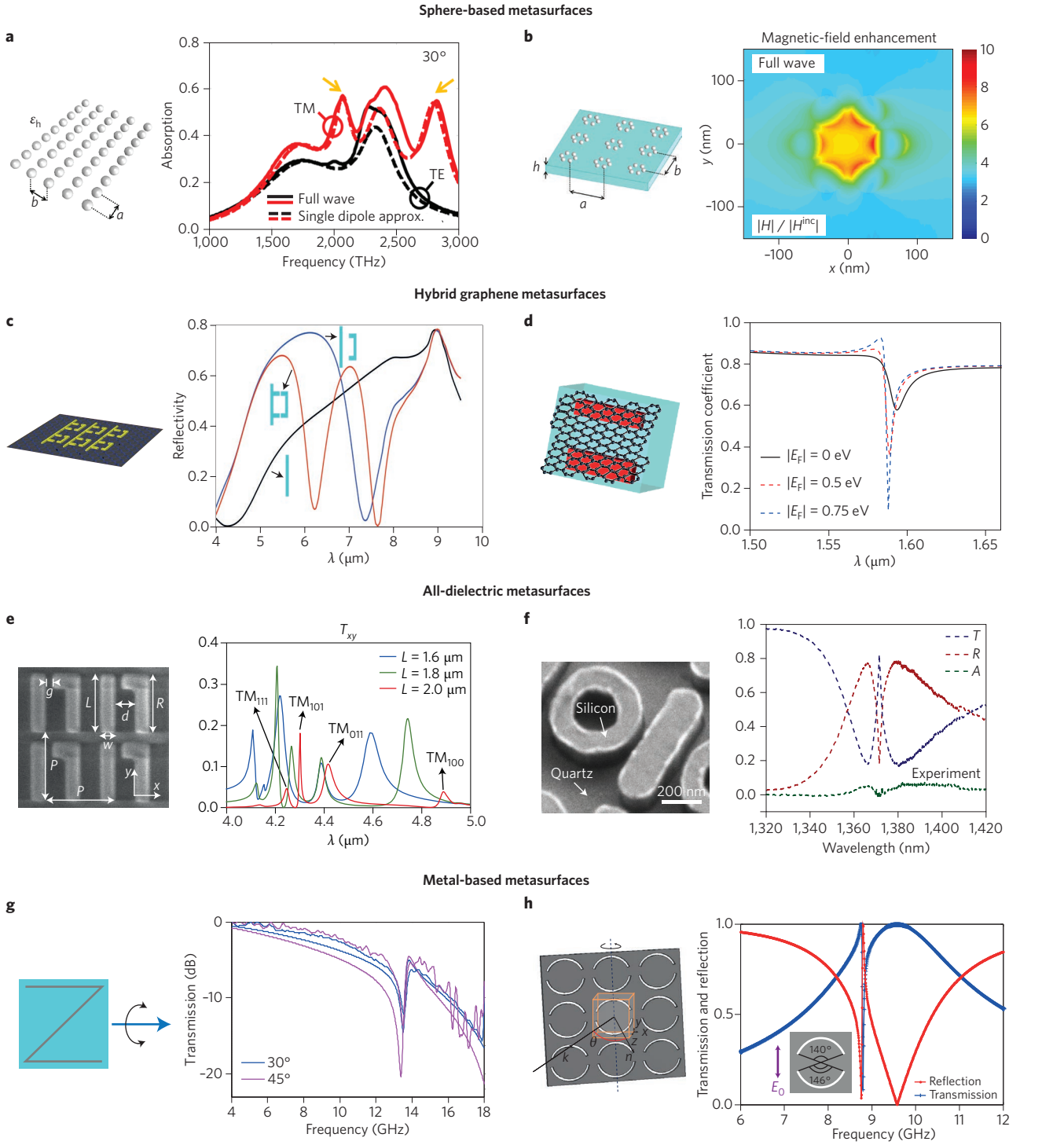


**Figure 5 | Fano resonances in metasurfaces. a**, An array of core–shell (sapphire in aluminium) nanoparticles and absorption spectra for the incidence angle of 30°. The yellow arrows point to array-dependent Fano resonances. TE, transverse electric polarization; TM transverse magnetic polarization; $\varepsilon_h$, permittivity; *a* and *b*, geometrical parameters. **b**, A metasurface composed of symmetric circular nanoclusters for the magnetic-field enhancement in a unit cell computed at a representative point of the magnetic Fano resonance. $H/H^{inc}$ is the magnetic field normalized by the incident magnetic field, and *a*, *b*, *h* are geometrical parameters. **c**, A Fano-resonant metasurface integrated with graphene and calculated reflectivity of normally incident *y*-polarized light for a wire grid (black), wire and C-shaped antenna (blue) and the full metasurface (red). **d**, A hybrid graphene/all-dielectric periodic metasurface and transmission coefficient for different doping levels of graphene. $E_F$, Fermi level. **e**, SEM image of the fabricated silicon-based chiral metasurface and measured cross-polarized transmission spectra $T_{xy}$ for different nanorod lengths *L*. **f**, SEM image of a single unit cell of the fabricated metasurface and measured transmittance (*T*), reflectance (*R*) and absorption (*A*) spectra. **g**, Schematic of a Z-shaped meta-atom and measured (dashed) and calculated (solid) transmission coefficient under 30° and 45° *H*-plane incidence. **h**, A metasurface consisting of an array of asymmetric split-ring apertures and calculated transmission and reflection spectra. The angle of incidence $\theta$ is measured between the incident wave vector *k* and the metasurface's surface normal *n*. Figure adapted from: **a**, ref. 97, AIP Publishing LLC; **b**, ref. 98, American Chemical Society; **c**, ref. 102, American Chemical Society; **d**, ref. 103, OSA; **e**, ref. 107, Macmillan Publishers Ltd; **f**, ref. 12, Macmillan Publishers Ltd; **g**, ref. 109, AIP Publishing LLC; **h**, ref. 110, AIP Publishing LLC.

Arrows in Fig. 5a mark the features that characterize metasurface-induced Fano resonances.

Magnetic Fano resonances were demonstrated for a metasurface composed of a periodic array of circular clusters of spherical nanoparticles as building blocks[98]. Similar to the case of a simple square metasurface[97], two kinds of narrow resonance were identified, and they are related either to single circular nanoclusters or an array-induced collective Fano resonance. The array-induced Fano resonances become narrower compared with resonances induced by a single cluster. The magnetic field spreads over a large area of the nanocluster while the electric field is concentrated mainly in the gaps between the neighbouring nanoparticles. The authors mention that similar narrow Fano resonances are expected for other geometries, such as nanodisks, and other materials, such as gold.

Also, we note here that the fabrication of nanospheres is a challenging task especially for dielectric particles with a large diameter. As a result, the measurements were performed for arrays of small plasmonic nanospheres[100]. In an experiment, the spheres have also been substituted by cylinders that are easier to fabricate but have similar optical properties[101].

**Hybrid graphene sheets.** Graphene, a 2D semi-metal with a linear dispersion, has appeared as a promising optoelectronic material with highly tunable optical properties[102–105]. However, in the important range of the telecom (near-infrared) wavelengths, its response is weak, which is a challenge for the development of graphene-based optical devices. Different all-dielectric and plasmonic structures (such as metamaterials, photonic crystals or waveguides) coupled to graphene have been proposed for the design of novel types of tunable photonic structure enabling amplitude and phase modulations[103]. In this active research area, metasurfaces are promising for integration with 2D graphene layers[102–105]. In such hybrid structures, the Fano resonance appears as the key phenomenon responsible for tunable coupling between graphene, metasurface modes and incoming electromagnetic radiation. Depending on the proposed configuration and design, different Fano regimes have been described theoretically and realized experimentally, including double Fano resonances[102] and cascaded Fano resonances[105].

A Fano-resonant metasurface integrated with a single layer of graphene (Fig. 5c) exhibits an optical response with two deep reflectivity minima due to Fano resonances, and therefore it can be characterized as a metasurface with a double EIT effect[102]. It was demonstrated experimentally and theoretically that due to Fano resonance, the metasurface dramatically enhances the interaction of infrared light with graphene. The Pauli blockage of interband transitions in graphene results in spectral shifts of the Fano resonances and reflectivity modulation by nearly one order of magnitude[102]. A schematic of a theoretically proposed metasurface that is composed of periodic pairs of asymmetric silicon nanobars of the subwavelength dimension hybridized with a graphene sheet is presented in Fig. 5d[103]. A sharp Fano-type resonance is observed due to the cancellation of the electric and magnetic dipole responses at a special frequency point.

**Dielectric metasurfaces.** Low-loss all-dielectric metasurfaces placed on different substrates (including a magnetized gyromagnetic ferrite substrate[106]) have been proposed and studied for different designs and applications[12,106–108]. One of the key ideas here is to employ the interaction between dark and bright mode resonances to produce a Fano resonance[21,28].

Fano-resonant metasurfaces based on Si and its oxides supporting optical resonances with high quality factors $Q > 100$ have been demonstrated experimentally[107]. Each unit cell is composed of one straight and one bent Si nanorod, where the bend is responsible for coupling between bright (electric dipole) and dark (electric quadrupole/magnetic dipole) resonances (Fig. 5e). Cross-polarized transmission $T_{xy}$ spectra provide the most remarkable evidence of the Fano interference: the baseline $T_{xy}$, small for all non-resonant wavelengths, dramatically increases at Fano resonances, as shown in Fig. 5e, because of the coupling of the dark modes to both $x$ and $y$ polarizations of the incident light. In addition, it was demonstrated experimentally that high (>50%) linear-to-circular polarization conversion efficiency can be achieved by making these metasurfaces chiral by design, opening possibilities for efficient ultrathin circular polarizers[107].

Another design of a Si-based metasurface employing Fano-resonant unit cells with the bright- and dark-mode resonators (Fig. 5f) was utilized to demonstrate the EIT effect[12]. Collective oscillations of the bar resonators form the bright mode resonance while the ring resonators interact through near-field coupling forming the dark mode. Owing to the low absorption loss and coherent interaction of the neighbouring meta-atoms, the peak of the transparency window of 82% at the wavelength of 1,371 nm with a $Q$ factor of 483 is observed experimentally, demonstrating the possibility to realize highly dispersive, low-loss, slow-light photonic devices[12].

**Plasmonic metasurfaces.** The Fano resonance has been studied extensively in different metal-based metasurfaces[109–111]. An interesting example is a metasurface composed of planar Z-shaped meta-atoms proposed as a design of the conventional LC resonators for achieving negative values of permittivity. Reflection and transmission spectra, calculated numerically and measured experimentally, demonstrate a dark (trapped) mode resonance that is associated with a Fano lineshape[109] (Fig. 5g).

An ultrathin Babinet-inverted metasurface composed of asymmetric split-ring apertures fabricated in a metal plate demonstrates a high-$Q$ Fano resonance and strong extrinsic chirality[110] (Fig. 5h). Importantly, the electromagnetic response of the metasurface can easily be tuned by the angle of incidence, and the $Q$ of the Fano resonance depends strongly on the asymmetry of the split-ring apertures and losses. We note that, in contrast to dielectric structures, metal-based metasurfaces are not scalable because in the gigahertz regime, the dissipation losses in metals are much lower, which explains the high $Q$ value of Fano resonances. However, metallic structures provide illustrative examples for the specific features of Fano resonances in metasurfaces.

## Perspectives and outlook

The Fano formula, first discovered in the studies of the Rydberg series for auto-ionization[1], has been applied to various spectroscopic problems and for different objects, practically without limitations. Owing to the deep insight it provides for spectroscopic data and its appearance in a broad range of nanophotonics studies, the Fano formula will continue to be a vital tool for optical design and analysis.

Recently, a non-trivial manifestation of Fano resonance in the time and frequency domains[7,112,113] has been analysed theoretically and observed experimentally across a variety of photonic phenomena. An educative example is a trapping and confining of the electromagnetic energy by the so-called bound states in the continuum (BICs). For any structure to support BICs, it should extend to infinity in at least one direction[114]. In compact photonic structures, a trapped state can manifest itself in the scattering spectrum as a sharp Fano resonance[47,48]. By changing the structural parameters or excitation conditions, one can observe that Fano resonances become sharper and eventually disappear when their $Q$ value tends to infinity near the quasi-BIC point ($Q \approx 10^6$; Fig. 6a). Therefore, the Fano resonance can be considered as a precursor of BICs, with unique properties that may lead to applications including optical sensors, filters and waveguides, as well as low-loss fibres and large-area lasers.

Very recently, the concept of Fano resonance appeared in the field of topological insulators[115] (Fig. 6b) and exotic states of light

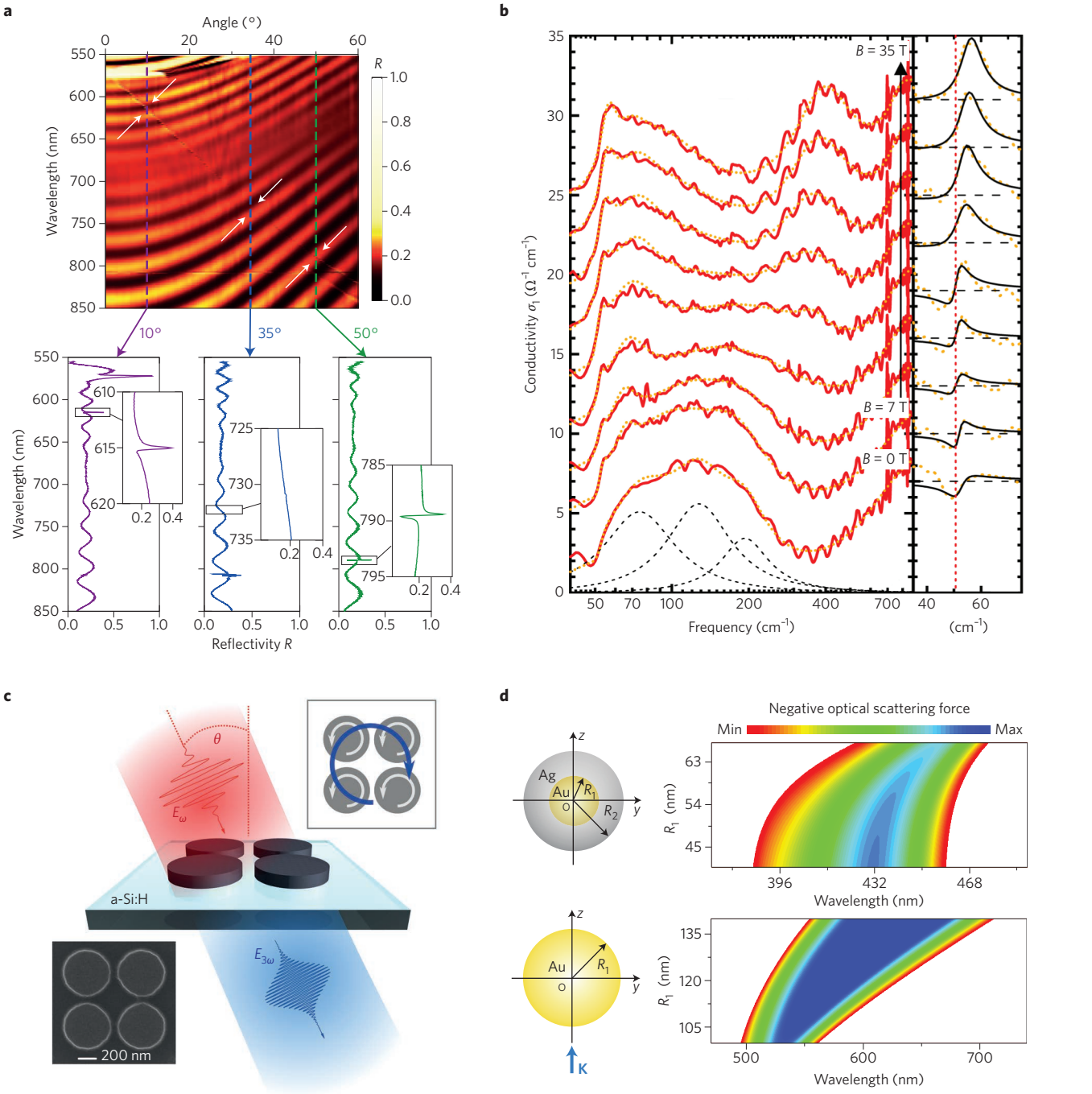


**Figure 6 | Recent examples of Fano resonances. a**, Top: experimentally measured reflectivity for *p*-polarized light along the $\Gamma$–$X$ direction of the photonic crystal slab. The feature of interest is the resonance (a thin faint line) extending from the top left corner to the bottom right corner. Bottom: slices at three representative angles, with close-ups near the resonance features. Disappearance of the resonance near 35° indicates a trapped state with no leakage. **b**, Left: the real part of the optical conductivity of $Bi_2Te_3$ as a function of the magnetic field ($B$) from 7 to 35 T. The conductivity mode located at ~50 $cm^{-1}$ invokes the asymmetric lineshape of a Fano resonance. Three Lorentzian modes (black dashed lines) are used to describe the broad spectral feature centred at ~150 $cm^{-1}$. Right: the Fano resonance is separated. The solid lines represent the best fits to the data using a Fano formula. **c**, Schematic of the resonant third-harmonic generation in the sample comprising a square array of symmetric clusters of four a-Si:H nanodisks (SEM image in the bottom left inset). Top right inset: origin of the magnetic Fano resonance in quadrumers — the coupled magnetic-like modes formed by out-of-plane magnetic dipoles and circulating displacement current produced by in-plane electric dipoles interfere destructively in the far-field. **d**, Phase diagrams of the longitudinal optical force in units of pN with respect to the incident wavelength and the particle size $R_1$ for a Au–Ag core–shell nanoparticle with fixed outer radius $R_2$ = 80 nm (top panel) and for a homogeneous Au nanoparticle (bottom panel). Coloured regions denote the parameter space to implement the negative optical scattering force phase exhibiting a red shift with an increase in particle radius, in accord with the Fano interference. **K**, wave vector. Figure reproduced from: **a**, ref. 47, Macmillan Publishers Ltd; **b**, ref. 115, APS; **c**, ref. 121, American Chemical Society; **d**, ref. 46, American Chemical Society.

including subwavelength topological photonics at the nanoscale[49]. The studies of topological insulator $Bi_2Se_3$ and phase transition in $(Bi_{1-x}In_x)_2Se_3$ triggered the analysis of topological Fano interference phenomena. Such Fano resonances can be tuned continuously, switched abruptly, modulated dynamically[116,117] and have been observed experimentally[118]. Topological effects can be realized in photonic crystals, coupled resonators, metamaterials and quasi-crystals[119]. In particular, for a crystal with time-reversal and particle–hole symmetries, it was demonstrated that an edge mode may couple to external modes via a Fano resonance[120].

For all-dielectric nanostructures, the magnetic Fano resonance was found to be crucially important in enhancing nonlinear optical effects[121], and the third-harmonic generation from dielectric nanoparticles has been observed experimentally (Fig. 6c). Non-trivial wavelength and angular dependencies of the generated harmonic radiation featured a maximum signal in the vicinity of the magnetic Fano resonance.

Fano resonance can provide a powerful tool to tailor the optical scattering force and even induce a net negative optical scattering force for plasmonic nanoparticles[46]. To achieve a negative force, a zeroth-order transverse-magnetic-polarized Bessel beam was used for the illumination, while plasmonic particles can have a core and shell, be homogeneous or even have a hollow (Fig. 6d). The underlying physical mechanism of the Fano-induced negative force originates from the simultaneous excitation of several multipoles, substantially enhancing the forward scattering via the Fano interference and leading to an increased backward recoil force that is superior to the forward incident force.

Very important are applications of Fano resonance in ultrasmall lasers based on interference between a continuum of waveguide modes and a discrete mode of a nanocavity[56], all-optical switching[51], identification of molecular monolayers[50], metamaterial absorbers with tunable resonances for broadband manipulation of mechanical resonances[57], spectral separation of optical spin angular momenta[52], nanofocusing beyond the diffraction limit[55], interferometric phase detectors[53], plasmonic colorimetric sensing[54], and so on. The realization of extremely small structures with a simple geometry and symmetry supporting Fano resonances is promising for data storage technology, sensing applications and topological optics[122]. The attractive property of small plasmonic particles is the coexistence of Fano resonance and singular optics effects[18,122], which allows control of optical vortices at the nanoscale. An intricate interconnection between far-field scattering and the near-field Poynting vector flux is manifested in the recently introduced concept of nano-Fano resonances[122].

Understanding the connection between Fano resonances[1], the Kerker effect[69] and EIT[11,12] is important for the design of robust optical devices with many applications in photonics and spectroscopy. In this Review, we have revealed that many essential resonant phenomena known in optics can be unified by a simple model of Fano resonance based on two coupled oscillators. We have presented a single phase diagram that shows an overlap of Fano, Kerker and EIT regimes and demonstrates a common background for seemingly different resonances in optics. We have explained the importance of the measurable and experimentally controllable Fano parameter $q$ (Fig. 4) that characterizes the asymmetry of the Fano lineshape and thus provides a route towards understanding and controlling interference processes across several branches of physics. Now it is clear that the seminal work[1] of Ugo Fano will remain one of the most cited papers in physics, as it is an influential source of exciting concepts for theoreticians, experimentalists and technologists with many possible applications proposed and yet to be implemented.

Received 22 June 2016; accepted 18 July 2017;
published online 1 September 2017

## References


1. Fano, U. Effects of configuration interaction on intensities and phase shifts. *Phys. Rev.* **124,** 1866–1878 (1961).
2. Fano, U. *Sullo spettro di assorbimento dei gas nobili presso il limite dello spettro darco. Il Nuovo Cimento* **12,** 154–161 (1935).
3. Connerade, J.-P. & Lane, A. M. Interacting resonances in atomic spectroscopy. *Rep. Prog. Phys.* **51,** 1439–1478 (1988).
4. Rybin, M. V., Filonov, D. S., Belov, P. A., Kivshar, Y. S. & Limonov, M. F. Switching from visibility to invisibility via Fano resonances: theory and experiment. *Sci. Rep.* **5,** 8774 (2015).
5. Rybin, M. V. *et al.* Mie scattering as a cascade of Fano resonances. *Opt. Express* **21,** 30107–30113 (2013).
6. Rybin, M. V. *et al.* Switchable invisibility of dielectric resonators. *Phys. Rev. B* **95,** 165119 (2017).
7. Ott, C. *et al.* Lorentz meets Fano in spectral line shapes: a universal phase and its laser control. *Science* **340,** 716–720 (2013).
8. Borrmann, G. *Die absorption von Röntgenstrahlen im fall der interferenz. Z. Phys.* **127,** 297–323 (1950).
9. Pettifer, R. F., Collins, S. P. & Laundy, D. Quadrupole transitions revealed by Borrmann spectroscopy. *Nature* **454,** 196–199 (2008).
10. Vinogradov, A. P. *et al.* Inverse Borrmann effect in photonic crystals. *Phys. Rev. B* **80,** 235106 (2009).
11. Peng, B., Özdemir, S. K., Chen, W., Nori, F. & Yang, L. What is and what is not electromagnetically induced transparency in whispering-gallery microcavities. *Nat. Commun.* **5,** 5082 (2014).
12. Yang, Y., Kravchenko, I. I., Briggs, D. P. & Valentine, J. All-dielectric metasurface analogue of electromagnetically induced transparency. *Nat. Commun.* **5,** 5753 (2014).
13. Yasir, K. A. & Liu, W.-M. Controlled electromagnetically induced transparency and Fano resonances in hybrid BEC-optomechanics. *Sci. Rep.* **6,** 22651 (2016).
14. Han, S. *et al.* Tunable electromagnetically induced transparency in coupled three-dimensional split-ring-resonator metamaterials. *Sci. Rep.* **6,** 20801 (2016).
15. Khunsin, W. *et al.* Quantitative and direct near-field analysis of plasmonic-induced transparency and the observation of a plasmonic breathing mode. *ACS Nano* **10,** 2214–2224 (2016).
16. Fong, K. Y., Fan, L., Jiang, L., Han, X. & Tang, H. X. Microwave-assisted coherent and nonlinear control in cavity piezo-optomechanical systems. *Phys. Rev. A* **90,** 051801 (2014).
17. Holfeld, C. P. *et al.* Fano resonances in semiconductor superlattices. *Phys. Rev. Lett.* **81,** 874–877 (1998).
18. Fan, P., Yu, Z., Fan, S. & Brongersma, M. L. Optical Fano resonance of an individual semiconductor nanostructure. *Nat. Mater.* **13,** 471–475 (2014).
19. Limonov, M. F., Rykov, A. I., Tajima, S. & Yamanaka, A. Raman scattering study on fully oxygenated $YBa_2Cu_3O_7$ single crystals: *x*–*y* anisotropy in the superconductivity-induced effects. *Phys. Rev. Lett.* **80,** 825–828 (1998).
20. Hadjiev, V. G. *et al.* Strong superconductivity-induced phonon self-energy effects in $HgBa_2Ca_3Cu_4O_{10+}\delta$. *Phys. Rev. B* **58,** 1043–1050 (1998).
21. Miroshnichenko, A. E., Flach, S. & Kivshar, Y. S. Fano resonances in nanoscale structures. *Rev. Mod. Phys.* **82,** 2257–2298 (2010).
22. Soboleva, I. V., Moskalenko, V. V. & Fedyanin, A. A. Giant Goos-Hänchen effect and Fano resonance at photonic crystal surfaces. *Phys. Rev. Lett.* **108,** 123901 (2012).
23. Yang, H. *et al.* Transfer-printed stacked nanomembrane lasers on silicon. *Nat. Photon.* **6,** 615–620 (2012).
24. Rybin, M. V. *et al.* Bragg scattering induces Fano resonance in photonic crystals. *Photon. Nanostruct. Fundam. Appl.* **8,** 86–93 (2010).
25. Zhou, W. *et al.* Progress in 2D photonic crystal Fano resonance photonics. *Progr. Quant. Electron.* **38,** 1–74 (2014).
26. Markoš, P. Fano resonances and band structure of two-dimensional photonic structures. *Phys. Rev. A* **92,** 043814 (2015).
27. Chong, K. E. *et al.* Observation of Fano resonances in all-dielectric nanoparticle oligomers. *Small* **10,** 1985–1990 (2014).
28. Luk'yanchuk, B. *et al.* The Fano resonance in plasmonic nanostructures and metamaterials. *Nat. Mater.* **9,** 707–715 (2010).
29. Rahmani, M., Luk'yanchuk, B. & Hong, M. Fano resonance in novel plasmonic nanostructures. *Laser Photon. Rev.* **7,** 329–349 (2013).
30. Vercruysse, D. *et al.* Directional fluorescence emission by individual V-antennas explained by mode expansion. *ACS Nano* **8,** 8232–8241 (2014).
31. Hopkins, B., Poddubny, A. N., Miroshnichenko, A. E. & Kivshar, Y. S. Circular dichroism induced by Fano resonances in planar chiral oligomers. *Laser Photon. Rev.* **10,** 137146 (2016).
32. Kraft, M., Luo, Y., Maier, S. A. & Pendry, J. B. Designing plasmonic gratings with transformation optics. *Phys. Rev. X* **5,** 031029 (2015).
33. Hopkins, B., Filonov, D. S., Glybovski, S. B. & Miroshnichenko, A. E. Hybridization and the origin of Fano resonances in symmetric nanoparticle trimers. *Phys. Rev. B* **92,** 045433 (2015).

34. He, J., Fan, C., Ding, P., Zhu, S. & Liang, E. Near-field engineering of Fano resonances in a plasmonic assembly for maximizing CARS enhancements. *Sci. Rep.* **6,** 20777 (2016).
35. Zhao, Q. *et al.* Experimental demonstration of isotropic negative permeability in a three-dimensional dielectric composite. *Phys. Rev. Lett.* **101,** 027402 (2008).
36. Huang, X., Lai, Y., Hang, Z. H., Zheng, H. & Chan, C. Dirac cones induced by accidental degeneracy in photonic crystals and zero-refractive-index materials. *Nat. Mater.* **10,** 582–586 (2011).
37. Ginn, J. C. *et al.* Realizing optical magnetism from dielectric metamaterials. *Phys. Rev. Lett.* **108,** 097402 (2012).
38. Moitra, P. *et al.* Realization of an all-dielectric zero-index optical metamaterial. *Nat. Photon.* **7,** 791–795 (2013).
39. Li, Y. *et al.* On-chip zero-index metamaterials. *Nat. Photon.* **9,** 738–742 (2015).
40. Kuznetsov, A. I., Miroshnichenko, A. E., Brongersma, M. L., Kivshar, Y. S. & Lukyanchuk, B. Optically resonant dielectric nanostructures. *Science* **354,** aag2472 (2016).
41. Ghenuche, P. *et al.* Optical extinction in a single layer of nanorods. *Phys. Rev. Lett.* **109,** 143903 (2012).
42. Yu, N. & Capasso, F. Flat optics with designer metasurfaces. *Nat. Mater.* **13,** 139–150 (2014).
43. Wang, F., Wei, Q.-H. & Htoon, H. Generation of steep phase anisotropy with zero-backscattering by arrays of coupled dielectric nano-resonators. *Appl. Phys. Lett.* **105,** 121112 (2014).
44. Olson, J. *et al.* High chromaticity aluminum plasmonic pixels for active liquid crystal displays. *ACS Nano* **10,** 1108–1117 (2016).
45. Ye, D., Lu, L., Joannopoulos, J. D., Soljačić, M. & Ran, L. Invisible metallic mesh. *Proc. Natl Acad. Sci. USA* **113,** 2568–2572 (2016).
46. Chen, H., Liu, S., Zi, J. & Lin, Z. Fano resonance-induced negative optical scattering force on plasmonic nanoparticles. *ACS Nano* **9,** 1926–1935 (2015).
47. Hsu, C. W. *et al.* Observation of trapped light within the radiation continuum. *Nature* **499,** 188–191 (2013).
48. Monticone, F. & Alu, A. Embedded photonic eigenvalues in 3D nanostructures. *Phys. Rev. Lett.* **112,** 213903 (2014).
49. Sinev, I. S. *et al.* Mapping plasmonic topological states at the nanoscale. *Nanoscale* **7,** 11904–11908 (2015).
50. Wu, C. *et al.* Fano-resonant asymmetric metamaterials for ultrasensitive spectroscopy and identification of molecular monolayers. *Nat. Mater.* **11,** 69–75 (2012).
51. Stern, L., Grajower, M. & Levy, U. Fano resonances and all-optical switching in a resonantly coupled plasmonic-atomic system. *Nat. Commun.* **5,** 4865 (2014).
52. Piao, X., Yu, S., Hong, J. & Park, N. Spectral separation of optical spin based on antisymmetric Fano resonances. *Sci. Rep.* **5,** 16585 (2015).
53. Heeg, K. P. *et al.* Interferometric phase detection at X-ray energies via Fano resonance control. *Phys. Rev. Lett.* **114,** 207401 (2015).
54. King, N. S. *et al.* Fano resonant aluminum nanoclusters for plasmonic colorimetric sensing. *ACS Nano* **9,** 10628–10636 (2015).
55. Song, M. *et al.* Nanofocusing beyond the near-field diffraction limit via plasmonic Fano resonance. *Nanoscale* **8,** 1635–1641 (2016).
56. Yu, Y., Xue, W., Semenova, E., Yvind, K. & Mork, J. Demonstration of a self-pulsing photonic crystal Fano laser. *Nat. Photon.* **11,** 81–84 (2017).
57. Zhu, H., Yi, F. & Cubukcu, E. Plasmonic metamaterial absorber for broadband manipulation of mechanical resonances. *Nat. Photon.* **10,** 709–714 (2016).
58. Joe, Y. S., Satanin, A. M. & Kim, C. S. Classical analogy of Fano resonances. *Phys. Script.* **74,** 259–266 (2006).
59. Verslegers, L., Yu, Z., Ruan, Z., Catrysse, P. B. & Fan, S. From electromagnetically induced transparency to superscattering with a single structure: a coupled-mode theory for doubly resonant structures. *Phys. Rev. Lett.* **108,** 083902 (2012).
60. Khanikaev, A. B., Wu, C. & Shvets, G. Fano-resonant metamaterials and their applications. *Nanophotonics* **2,** 247–264 (2013).
61. Finch, M. F. & Lail, B. A. Multi-coupled resonant splitting with a nano-slot metasurface and PMMA phonons. In *Proc. SPIE 9547, Plasmonics: Metallic Nanostructures and Their Optical Properties XIII* 954710 (eds Boardman, A. D. & Tsai, D. P.) (SPIE, 2015).
62. Khitrova, G., Gibbs, H. M., Kira, M., Koch, S. W. & Scherer, A. Vacuum Rabi splitting in semiconductors. *Nat. Phys.* **2,** 81–90 (2006).
63. Purcell, E. M. Spontaneous emission probabilities at radio frequencies. *Phys. Rev.* **69,** 681 (1946).
64. Lamb, W. E. & Retherford, R. C. Fine structure of the hydrogen atom by a microwave method. *Phys. Rev.* **72,** 241–243 (1947).
65. Novikov, V. B. & Murzina, T. V. Borrmann effect in photonic crystals. *Opt. Lett.* **42,** 1389–1392 (2017).
66. Barreaux, J. L. P. *et al.* Narrowband and tunable anomalous transmission filters for spectral monitoring in the extreme ultraviolet wavelength region. *Opt. Express* **25,** 1993–2008 (2017).
67. Rybin, M. V. *et al.* Fano resonances in antennas: general control over radiation patterns. *Phys. Rev. B* **88,** 205106 (2013).
68. Kerker, M., Wang, D.-S. & Giles, C. L. Electromagnetic scattering by magnetic spheres. *J. Opt. Soc. Am.* **73,** 765–767 (1983).
69. Geffrin, J.-M. *et al.* Magnetic and electric coherence in forward-and back-scattered electromagnetic waves by a single dielectric subwavelength sphere. *Nat. Commun.* **3,** 1171 (2012).
70. Niemi, T., Karilainen, A. O. & Tretyakov, S. A. Synthesis of polarization transformers. *IEEE Trans. Antennas Propag.* **61,** 3102–3111 (2013).
71. Kavokin, A., Baumberg, J. J., Malpuech, G. & Laussy, F. P. *Microcavities* (Oxford Univ. Press, 2007).
72. Yoshino, S., Oohata, G. & Mizoguchi, K. Dynamical Fano-like interference between Rabi oscillations and coherent phonons in a semiconductor microcavity system. *Phys. Rev. Lett.* **115,** 157402 (2015).
73. Feng, L., Wong, Z. J., Ma, R.-M., Wang, Y. & Zhang, X. Single-mode laser by parity-time symmetry breaking. *Science* **346,** 972–975 (2014).
74. Bender, C. M. & Boettcher, S. Real spectra in non-Hermitian Hamiltonians having *PT* symmetry. *Phys. Rev. Lett.* **80,** 5243–5246 (1998).
75. Rüter, C. E. *et al.* Observation of parity–time symmetry in optics. *Nat. Phys.* **6,** 192–195 (2010).
76. Peng, B. *et al.* Parity-time-symmetric whispering-gallery microcavities. *Nat. Phys.* **10,** 394–398 (2014).
77. Harari, G. *et al.* Topological insulators in PT-symmetric lattices. In *CLEO: 2015* paper FTh3D.3 (Optical Society of America, 2015).
78. Weimann, S. *et al.* Topologically protected bound states in photonic parity–time-symmetric crystals. *Nat. Mater.* **16,** 433–438 (2016).
79. Zyablovsky, A. A., Vinogradov, A. P., Pukhov, A. A., Dorofeenko, A. V. & Lisyansky, A. A. PT symmetry in optics. *Phys. Usp.* **57,** 1063–1082 (2014).
80. Suchkov, S. V. *et al.* Nonlinear switching and solitons in PT-symmetric photonic systems. *Laser Photon. Rev.* **10,** 177–213 (2016).
81. Hopkins, B., Poddubny, A. N., Miroshnichenko, A. E. & Kivshar, Y. S. Revisiting the physics of Fano resonances for nanoparticle oligomers. *Phys. Rev. A* **88,** 053819 (2013).
82. Fan, S., Suh, W. & Joannopoulos, J. D. Temporal coupled-mode theory for the Fano resonance in optical resonators. *J. Opt. Soc. Am. A* **20,** 569–572 (2003).
83. Poddubny, A. N., Rybin, M. V., Limonov, M. F. & Kivshar, Y. S. Fano interference governs wave transport in disordered systems. *Nat. Commun.* **3,** 914 (2012).
84. Tribelsky, M. I. & Miroshnichenko, A. E. Giant in-particle field concentration and Fano resonances at light scattering by high-refractive index particles. *Phys. Rev. A* **93,** 053837 (2016).
85. Kong, X. & Xiao, G. Fano resonance in high-permittivity dielectric spheres. *J. Opt. Soc. Am. A* **33,** 707–711 (2016).
86. Rybin, M. V., Mingaleev, S. F., Limonov, M. F. & Kivshar, Y. S. Purcell effect and Lamb shift as interference phenomena. *Sci. Rep.* **6,** 20599 (2016).
87. Mie, G. *Beiträge zur optik trüber medien, speziell kolloidaler metallösungen. Ann. Phys.* **330,** 377–445 (1908).
88. Miroshnichenko, A. E. *et al.* Fano resonances: a discovery that was not made 100 years ago. *Opt. Photon. News* **19,** 48 (2008).
89. Kong, X. & Xiao, G. Fano resonances in core-shell particles with high permittivity covers. In *2016 Progress in Electromagnetic Research Symposium (PIERS)* 1715–1719 (PIERS, 2016).
90. Rybin, M. V. *et al.* Fano resonance between Mie and Bragg scattering in photonic crystals. *Phys. Rev. Lett.* **103,** 023901 (2009).
91. Pariente, J. A. *et al.* Percolation in photonic crystals revealed by Fano resonance. Preprint at http://arXiv.org/abs/1607.08890 (2016).
92. Ricciardi, A. *et al.* Evidence of guided resonances in photonic quasicrystal slabs. *Phys. Rev. B* **84,** 085135 (2011).
93. Limonov, M. F. & De La Rue, R. M. (eds) *Optical Properties of Photonic Structures: Interplay of Order and Disorder* (CRC Press, 2012).
94. Fan, S. Sharp asymmetric line shapes in side-coupled waveguide-cavity systems. *Appl. Phys. Lett.* **80,** 908–910 (2002).
95. Yu, P. *et al.* Fano resonances in ultracompact waveguide Fabry-Perot resonator side-coupled lossy nanobeam cavities. *Appl. Phys. Lett.* **103,** 091104 (2013).
96. Vlasov, Y. A., Bo, X.-Z., Sturm, J. C. & Norris, D. J. On-chip natural assembly of silicon photonic bandgap crystals. *Nature* **414,** 289–293 (2001).
97. Campione, S. *et al.* Fano collective resonance as complex mode in a two-dimensional planar metasurface of plasmonic nanoparticles. *Appl. Phys. Lett.* **105,** 191107 (2014).
98. Campione, S., Guclu, C., Ragan, R. & Capolino, F. Enhanced magnetic and electric fields via Fano resonances in metasurfaces of circular clusters of plasmonic nanoparticles. *ACS Photon.* **1,** 254–260 (2014).
99. Sharac, N. *et al.* Tunable optical response of bowtie nanoantenna arrays on thermoplastic substrates. *Nanotechnology* **27,** 105302 (2016).
100. Aristov, A. I. *et al.* Laser-ablative engineering of phase singularities in plasmonic metamaterial arrays for biosensing applications. *Appl. Phys. Lett.* **104,** 071101 (2014).
101. Paniagua-Domnguez, R. *et al.* Generalized Brewster effect in dielectric metasurfaces. *Nat. Commun.* **7,** 10362 (2016).

102. Dabidian, N. *et al.* Electrical switching of infrared light using graphene integration with plasmonic Fano resonant metasurfaces. *ACS Photon.* **2,** 216–227 (2015).
103. Argyropoulos, C. Enhanced transmission modulation based on dielectric metasurfaces loaded with graphene. *Opt. Express* **23,** 23787–23797 (2015).
104. Mousavi, S. H. *et al.* Inductive tuning of Fano-resonant metasurfaces using plasmonic response of graphene in the mid-infrared. *Nano Lett.* **13,** 1111–1117 (2013).
105. Smirnova, D. A., Miroshnichenko, A. E., Kivshar, Y. S. & Khanikaev, A. B. Tunable nonlinear graphene metasurfaces. *Phys. Rev. B* **92,** 161406 (2015).
106. Mousavi, S. H., Khanikaev, A. B., Allen, J., Allen, M. & Shvets, G. Gyromagnetically induced transparency of metasurfaces. *Phys. Rev. Lett.* **112,** 117402 (2014).
107. Wu, C. *et al.* Spectrally selective chiral silicon metasurfaces based on infrared Fano resonances. *Nat. Commun.* **5,** 3892 (2014).
108. Yang, Y. *et al.* Nonlinear Fano-resonant dielectric metasurfaces. *Nano Lett.* **15,** 7388–7393 (2015).
109. Dhouibi, A., Burokur, S. N., Lupu, A., de Lustrac, A. & Priou, A. Excitation of trapped modes from a metasurface composed of only Z-shaped meta-atoms. *Appl. Phys. Lett.* **103,** 184103 (2013).
110. Wang, F., Wang, Z. & Shi, J. Theoretical study of high-*Q* Fano resonance and extrinsic chirality in an ultrathin Babinet-inverted metasurface. *J. Appl. Phys.* **116,** 153506 (2014).
111. Monticone, F. & Alu, A. Metamaterials and plasmonics: from nanoparticles to nanoantenna arrays, metasurfaces, and metamaterials. *Chin. Phys. B* **23,** 047809 (2014).
112. Ott, C. *et al.* Reconstruction and control of a time-dependent two-electron wave packet. *Nature* **516,** 374–378 (2014).
113. Kotur, M. *et al.* Spectral phase measurement of a Fano resonance using tunable attosecond pulses. *Nat. Commun.* **7,** 10566 (2016).
114. Hsu, C. W., Zhen, B., Stone, A. D., Joannopoulos, J. D. & Soljačić, M. Bound states in the continuum. *Nat. Rev. Mater.* **1,** 16048 (2016).
115. Tung, L.-C. *et al.* Magnetoinfrared spectroscopic study of thin $Bi_2Te_3$ single crystals. *Phys. Rev. B* **93,** 085140 (2016).
116. Autore, M. *et al.* Plasmon–phonon interactions in topological insulator microrings. *Adv. Opt. Mater.* **3,** 1257–1263 (2015).
117. Sim, S. *et al.* Ultrafast terahertz dynamics of hot Dirac-electron surface scattering in the topological insulator $Bi_2Se_3$. *Phys. Rev. B* **89,** 165137 (2014).
118. Glinka, Y. D., Babakiray, S., Holcomb, M. B. & Lederman, D. Effect of Mn doping on ultrafast carrier dynamics in thin films of the topological insulator $Bi_2Se_3$. *J. Phys. Condens. Matter* **28,** 165601 (2016).
119. Lu, L., Joannopoulos, J. D. & Soljačić, M. Topological photonics. *Nat. Photon.* **8,** 821–829 (2014).
120. Atherton, T. J. *et al.* Topological modes in one-dimensional solids and photonic crystals. *Phys. Rev. B* **93,** 125106 (2016).
121. Shorokhov, A. S. *et al.* Multifold enhancement of third-harmonic generation in dielectric nanoparticles driven by magnetic Fano resonances. *Nano Lett.* **16,** 4857–4861 (2016).
122. Luk'yanchuk, B. S., Miroshnichenko, A. E. & Kivshar, Y. S. Fano resonances and topological optics: an interplay of far-and near-field interference phenomena. *J. Opt.* **15,** 073001 (2013).


## Acknowledgements

We thank P. Belov, S. Flach, B. Hopkins, A. A. Kaplyansky, B. Luk'yanchuk and M. Scully for useful discussions and suggestions, and D. Powell for critical reading of the manuscript. We acknowledge financial support from the Russian Science Foundation (grant 15-12-00040) and the Australian Research Council.

## Additional information

Reprints and permissions information is available online at www.nature.com/reprints. Publisher's note: Springer Nature remains neutral with regard to jurisdictional claims in published maps and institutional affiliations. Correspondence should be addressed to M.V.R.

## Competing financial interests

The authors declare no competing financial interests.